ORIGINAL RESEARCH

Construction and Application of a PD-L1-Targeted Multimodal Diagnostic and Dual-Functional Theranostics Nanoprobe

Chengxue He[1,2,*], YanHui Guo[3,*], Nina Zhou[2,*], Zhen Wang[4,*], Teli Liu[2], Xiaoxia Xu[2], Feng Wang[2], Hua Zhu[2], Zhi Yang[1,2], Xianteng Yang[1,5], Lei Xia [ID][2]

[1]Medical College, Guizhou University, Guiyang, GuiZhou Province, People's Republic of China; [2]Key Laboratory of Carcinogenesis and Translational Research (Ministry of Education/Beijing), NMPA Key Laboratory for Research and Evaluation of Radiopharmaceuticals (National Medical Products Administration), Department of Nuclear Medicine, Peking University Cancer Hospital & Institute, Beijing, People's Republic of China; [3]Department of Radiology, Peking University Third Hospital, Beijing, People's Republic of China; [4]Key Laboratory of Carcinogenesis and Translational Research (Ministry of Education, Beijing), Department of Hepato-Pancreato-Biliary Surgery, Sarcoma Center, Peking University Cancer Hospital & Institute, Beijing, People's Republic of China; [5]Department of Orthopedics, Guizhou Provincial People's Hospital, Guiyang, GuiZhou Province, People's Republic of China

*These authors contributed equally to this work

Correspondence: Lei Xia; Zhi Yang, Tel +86 010-88197852; +86 010-88196196, Email xialei9012288@126.com; pekyz@163.com

Background: In recent years, PD-L1 has been primarily utilized as an immune checkpoint marker in cancer immunotherapy. However, due to tumor heterogeneity, the response rate to such therapies often falls short of expectations. In addition to its role in immunotherapy, PD-L1 serves as a specific target on the surface of tumor cells for targeted diagnostic and therapeutic interventions. There is an absence of a fully developed PD-L1-targeted diagnostic and therapeutic probe for clinical use, which constrains the exploration and clinical exploitation of this target.

Methods and Results: In this study, we engineered a PD-L1-targeted probe with multimodal imaging and dual therapeutic functionalities utilizing organic melanin nanoparticles. Functionalization with the WL12-SH peptide endowed the nanoprobe with specific targeting capabilities. Subsequent radiolabeling with ^{89}Zr (half-life: 100.8 hours) and chelation of Mn^{2+} ions afforded the probe the capacity for simultaneous PET and MRI imaging modalities. Cellular uptake assays revealed pronounced specificity, with -positive cells exhibiting significantly higher uptake than -negative counterparts ($p < 0.05$). Dual-modal PET/MRI imaging delineated rapid and sustained accumulation at the neoplastic site, yielding tumor-to-non-tumor (T/NT) signal ratios at 24 hours post-injection of 16.67 ± 3.45 for PET and 6.63 ± 0.64 for MRI, respectively. We conjugated the therapeutic radionuclide ^{131}I (half-life: 8.02 days) to the construct and combined low-dose radiotherapy and photothermal treatment (PTT), culminating in superior antitumor efficacy while preserving a high safety profile. The tumors in the cohort receiving the dual-modality therapy exhibited significantly reduced volume and weight compared to those in the control and monotherapy groups.

Conclusion: We developed and applied a novel -targeted multimodal theranostic nanoprobe, characterized by its high specificity and superior imaging capabilities as demonstrated in PET/MRI modalities. Furthermore, this nanoprobe facilitates potent therapeutic efficacy at lower radionuclide doses when used in conjunction with PTT.

Keywords: theranostics, PET/MRI, melanin nanoparticles, photothermal therapy

Introduction

Currently, various methods have been developed for malignant tumors, including surgery, chemotherapy, targeted therapy, radiotherapy, and immunotherapy, which has been applied as a standardized method in tumor treatment. Among them, immune checkpoint inhibitors targeting cytotoxic T lymphocyte-associated protein 4 (CTLA-4) and programmed cell death protein 1/programmed cell death ligand 1 (PD-1/) have been applied to various tumors such as advanced melanoma, Merkel cell carcinoma, and non-small cell lung cancer.[1–3] Although immune checkpoint inhibitors have the potential to revolutionize tumor treatment, the effects shown in preliminary clinical trials are not entirely satisfactory. Some research has shown that

Graphical Abstract
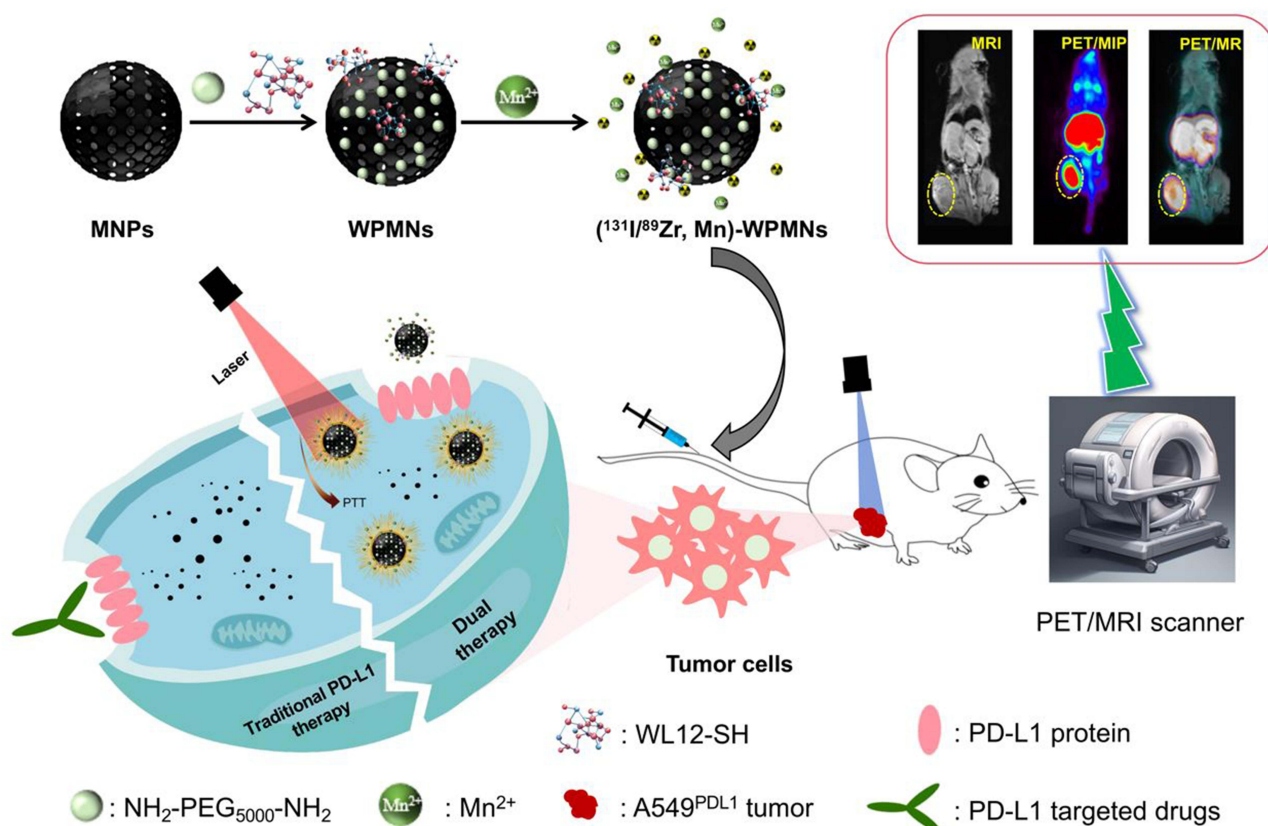
only a subset of patients treated with immune checkpoint inhibitors respond positively.[1] In addition, as a tumor cell-specific target, PD-L1 is widely expressed on the surface of multiple tumor cells.[4] The expression rate of PD-L1 differs significantly across various tumor types, studies have discovered that in non-small cell lung cancer, its expression rate ranges from approximately 20% to 50%, PD-L1 gradually being used as a specific target for tumor-specific diagnosis and treatment.[5–7]

A considerable proportion of patients receiving PD-1/PD-L1 treatment may ultimately develop treatment resistance.[8–10] This is due to both the presence of primary resistance and the development of acquired resistance in some patients with sustained responses.[11,12] Tumor-intrinsic factors such as PD-L1 expression, mutation burden, and antigen presentation defects are several factors extensively studied and can lead to the development of resistance.[13–15] The combination of multiple drugs or therapies methods can partially prevent or delay the occurrence of resistance. For example, the combination of a PD-1-targeted monoclonal antibody nivolumab and CTLA4-targeted monoclonal antibody ipilimumab for the treatment of advanced melanoma had overall survival for more than 60.0 months compared with 36.9 months in the nivolumab group and 19.9 months in the ipilimumab group.[16] While combination therapy can achieve better results, it may also correspondingly result in serious toxic side effects as the dosage of each individual drug is not immediately reduced.[17] Currently, the combination of multiple therapies has become a common choice for the treatment of malignant tumors, such as radiotherapy and chemotherapy combinations, surgery and chemotherapy combinations, etc.[18,19] Previous studies have shown that combining different treatment methods can reduce the dosage of each individual therapy without affecting treatment efficacy, while reducing toxicity and potentially achieving a synergistic effect.[20] Therefore, it is expected that targeting tumors using PD-L1 as a specific target for radionuclide therapy combined with photothermal therapy may achieve better therapeutic results.

WL12 is a selected peptide molecule that targets, featuring the advantages of small molecules combined with a higher affinity. Some research used the peptide WL12 to label the positron short half-life radioactive nuclide ^{68}Ga to construct a -targeted PET imaging probe named ^{68}Ga-NOTA-WL12 and conducted clinical translational research. The results showed that ^{68}Ga-NOTA-WL12 displayed targeted PET imaging function and could be used for non-invasive detection of the expression level of in primary and metastatic lesions.[21] Our previous study had attempted to use organic melanin nanoparticles carrying WL12-SH (WL12 peptide modified with mercaptopropionic acid) peptide to construct a targeted enhanced PET imaging probe, which showed better targeting effects than small molecule probes, while also exhibiting long retention time at the tumor site, providing a reference for subsequent targeted tumor research.[22] Additionally, PET/MRI have achieved great value in the diagnosis of malignant tumors as a new type of nuclear medicine equipment.[23,24] But only PET/MRI diagnosis cannot replace contrast-enhanced imaging. Most patients still need to scan enhanced-MRI after PET/MRI examination with conventional contrast agent and strict enhanced-time.[25] Therefore, a PET/MRI dual-modality contrast agent to reduce the number of injections for patients and potentially utilize the characteristics of new contrast agents to flexibly adjust scanning time for better images is necessary. Some studies have attempted to construct PET and MRI dual contrast molecular probes and conducted basic research.[26–28] Our previous research has successfully constructed a prostate cancer-targeted PET/MRI dual-modality imaging probe by leveraging the intrinsic photoacoustic imaging capabilities of melanin nanoparticles and the metal-coupling functionalities, as well as their abundant surface-active groups. During this period, we leveraged the high compatibility of melanin nanoparticles to construct a broadly applicable PD-L1-targeted probe for PET/MRI dual-modality enhancement, which is feasible and will benefit more patients.[22]

Therefore, our study has continuously improved the function and application scenarios of the probe on the basis of building PD-L1 targeted PET imaging probe. We used the high-loading function of melanin nanoparticles to label positron nuclide [89]Zr ($^{1/2}$t=78.4 h) for PET imaging with higher radiolabeling rate, paramagnetic metal particle Mn^{2+} for enhanced MR imaging, and attempted to label therapeutic nuclide ^{131}I, which can be transmitted β radiation for killing tumor cells. Photothermal therapy (PTT) is a minimally invasive therapeutic approach by leveraging the principle of photothermal conversion. Together with the photothermal treatment function of melanin nanoparticles, this nanoprobe can be used for PET/MRI dual-modality enhanced imaging of PD-L1 overexpressed tumors, improving diagnostic sensitivity and image resolution. Concurrently, the probe facilitates a synergistic treatment paradigm by combining radionuclide therapy with photothermal therapy, potentially achieving enhanced therapeutic outcomes with reduced dosages. This study is set to broaden the scope of PD-L1 targeting applications and furnish novel insights for the management of tumors overexpressing PD-L1, particularly in cases exhibiting drug resistance.

Materials and Methods
Materials
Majority of the reagents for synthesizing melanin nanoparticles (MNPs) and PEG-MNPs were purchased from Sigma Aldrich (St. Louis, Missouri, USA), including melanin, sodium hydroxide and hydrochloric acid. WL12-SH was obtained from Tanzhen Bio (Nanchang, China). All the reagents of cell culture were obtained from Biological Industries (Beijing, China). The production and purification of radionuclide [89]Zr were provided by the Nuclear Medicine Cyclotron Group of Peking University Cancer Hospital. The radioactive nuclide ^{131}I purchased from Atomic High Tech (Beijing, China).

Synthesis, Characterization and Stability of Mn-WPMNs
WL12-SH modified melanin nanoparticles (WPMNs) were synthesized based on previously reported methods.[1] In short, we modified PEG-MNP by WL12-SH on PEG-MNPs (the ratio of PEG-MNP to WL12-SH was 1:19), adding aminosulfhydryl crosslinking agent sulfo-SMCC (5 µmol) and reacting overnight to obtain the final product after purification. 1 mg WPMN and excessive $MnCl_2$ (The ratio of WPMN to $MnCl_2$ was 1:100) were mixed and stirred overnight, obtaining the Mn-WPMN after purifying with PD-10 and ultrafiltration with 10 kDa ultrafiltration tube. MNP and WPMN with a concentration of 0.5 mg/mL were dropped onto a copper mesh for drying to prepare the sample. The WPMN morphological image was acquired by JEM-2100F Transmission electron microscopy under 200 kV acceleration voltage. Using dynamic light scattering (DLS) technology, the hydrodynamic diameters of MNPs, WMNPs, and Mn-WPMNs were measured using a laser light scattering

spectrometer (SLS-5022F, Germany). Detection of infrared spectra of MNPs and WPMNs using a 600 MHz nuclear magnetic resonance (Bruker) spectrometer. To evaluate the stability of the Mn-WPMNs in vitro, the Mn-WPMNs were co-incubated with 0.01 M PBS and 5% HSA at room temperature. 0.01 M PBS and 5% HSA solutions were dialyzed at 2, 24, 48, 72, and 96 h using 10 kDa dialysis tubes. The dialysate was collected to further analysis using ICP-MS.

Radioactive Labeling and Quality Control of (^{89}Zr, Mn)-WPMNs

For ^{89}Zr labeling, 0.1 M HEPES and 2M Na_2CO_3 solution were added in 37MBq ^{89}Zr-OXA acid solution to adjust the PH to 7.0, and then 1mg Mn-WPMNs added and reacted at 60°C for 1h. Using PD-10 column to purify and obtain the final product. (^{89}Zr, Mn)-WPMNs added in 0.01 M PBS and 5% HSA to detect the vitro stability at 0, 2, 24, 48, 72, 96 h by Radio-TLC.

For ^{131}I labeling, we added 1 mg WPMNs to 37 MBq ^{131}I solution with 0.1 M phosphate buffer (PB) and 40 μL of 1mg/mL N-Bromosuccinimide (NBS), and reacted 1 min at room temperature. Using PD-10 column to purify and obtain the final product of ^{131}I-WPMNs.

Cells and Mouse Model

All animal experiments have passed the Ethics Review Committee of Peking University Cancer Hospital and strictly follows the principles outlined in the Experimental Animal Ethics Committee of Peking University Cancer Hospital. The A549 cells were purchased from American Type Culture Collection (ATCC). A549[PD-L1] cells of high PDL1 expression obtained from our laboratory and cultured in RPMI-1640 medium with 10% Fetal Bovine Serum and 1% Penicillin-Streptomycin at 37°C with 5% CO_2. For the mouse models building, 4~5 weeks balb/c-nude were injected 1×10^5 cells in right thigh. Experimental research started after the tumor diameter reached around 0.5–0.8cm.

Cell Uptake and Internalization Analysis

The day before the experiment, A549[PD-L1] cells were cultured in a 24 well plate with 2×10^5 cells per well and incubated at 37°C with 5% CO_2. The 24 well plate was washed with 0.01M cold PBS of several times. For cell uptake study, 74KBq (^{89}Zr, Mn)-WPMNs added per well and incubated at 10, 30, 60, 120min in 37°C with 5% CO_2 (n = 4). The blocking group, 20 μg precursor (Mn-WPMNs) and (^{89}Zr, Mn)-WPMNs were co-incubated at 60 and 120min. Discarded the solution and washed several times with PBS at each time. The cells were lysate by 200 μL 1M NaOH, and then collected to analysis by γ-counter.

For the internalization study, 37 KBq (^{89}Zr, Mn)-WPMNs with 500 μL RPMI-1640 medium was added in the 24 well plate and incubated 1h at 37°C and 4°C. The 1640 medium was added in the 24 well plate and collected at 0, 30, 60, 120, 240min as the dissociation part. 500 μL 0.1 M acetic acid (dissolved in 0.01 M PBS pH: 5) added and incubated for 5 minutes before collecting as the membrane binding part; The internalized portion of the radioactive marker was cleaved and collected using 500 μL 1 M NaOH. All parts were measured by γ-counter.

Pharmacokinetics and Distribution of (^{89}Zr, Mn)-WPMNs

For the pharmacokinetics study, 5-weeks-old healthy KM mouses were injected 0.74 MBq (^{89}Zr, Mn)-WPMNs though the tail vein. Blood samples were collected from orbital vein at 1, 3, 5, 10, 15, 20, 30, 45 min and 1, 1.5, 2, 3, 4, 14, 24, 48, 72, 96 h, and measured by a γ-counter after weighing.

For the biodistribution study, fifteen 5-weeks-old healthy KM mice were randomly divided into 5 groups. All mice were injected 0.74 MBq (^{89}Zr, Mn)-WPMNs and executed at 2, 24, 48, 72, 96 h. The organs including blood, heart, liver, spleen, lung, kidney, stomach, small intestine, large intestine, muscle, bone and brain were taken out and detected by a γ-counter after weighing.

Micro-PET/CT Imaging in Tumor Model

A549[PD-L1] tumor bearing mice and the Micro-PET/CT system (SuperNova, PINGSENG Healthcare, China) were used to imaging study. The mice were injected 3.7 MBq (^{89}Zr, Mn)-WPMNs, and the PET/CT images of scanning 15min were collected by 2, 4, 24, 48, 72, 96 h while the mice were maintaining anesthesia with 1.5% isoflurane anesthesia gas. Attenuation correction reconstruction (CT ac reconstruction) was performed based on CT data after image acquisition

was completed. The maximum single-voxel standardized uptake value of the organs (heart, liver, lung, muscle, bone, brain, tumor) based on CT data for drawing regions of interest (ROI).

PET/MRI in vivo and MRI in vitro

In order to test the t1 weighted imaging function of Mn-WPMNs, Mn-WPMNs aqueous solution and common t1 weighted contrast agent Gd-DTPA with different concentrations (0.0625, 0.125, 0.25, 0.5, 1 mg/mL) were mixed with 1% agarose gel respectively for in vitro magnetic resonance imaging. Using a clinical 1.5T magnetic resonance scanner (Siemens, Germany) with animal micro-coils. The MRI sequence was as follows: TR: 531 ms, TE: 9.1 ms; Flip angle 30 °; Field of view: 160×100 square millimeters; Matrix: 256 × 256; Slice thickness: 3 millimeters. After processing the image using ImageJ software, calculate the R1 value (1/T1 (s-1)) and curve fitting results.

A549^{PD-L1} tumor bearing mice with or without Mn-WPMNs blocking were scanned with PET/MRI after the mice were administered peritoneal injection 200 μL of 4% chloral hydrate to narcotism. PET/MRI images were collected at 2, 24, 72, 96h by using a clinical 3.0T MR scanner (United Imaging, China) with an animal micro-coil after injecting 3.7 MBq (^{89}Zr, Mn)-WPMNs through the tail vein. The analysis of the MR signal in the tumor images was conducted with 3D slice software.

Toxicity Studies

To detect whether ^{131}I-WPMNs have toxicity in vivo. Ten 5-weeks-old KM mice were randomly divided two group as experimental and control. The experimental group was injected 200 μL of 1mg WPMNs labeled with 1mCi ^{131}I and the control group were injected same volume PBS. The weight of mice was measured every two days for 20 days. On the last day, the experimental and control group were executed and removed important organs (heart, liver, spleen, lung, kidney, stomach, intestine, brain) for hematoxylin-eosin (HE) staining.

Therapy Study in A549^{PD-L1} Model

The treatment study was conducted using A549^{PD-L1} tumor-bearing mice. 25 female A549^{PD-L1} tumor-bearing mice, aged 4–5 weeks, with tumor growth for one week, were randomly divided into 5 groups: control group, ^{131}I group, Laser group, ^{131}I-WPMNs group, and ^{131}I-WPMNs + Laser group. 1) Control group: each tumor-bearing mouse was injected with 200 μL 0.01M PBS via tail vein; 2) ^{131}I group: each tumor-bearing mouse was injected with ^{131}I diluted with 0.01 M PBS via tail vein (11.1 MBq, 200 μL); 3) Laser group: each tumor-bearing mouse was injected with 200 μL of 0.01 M PBS through the tail vein. After 24 h, each mouse underwent infrared laser treatment at the tumor site for 20 min (emission wavelength 808 nm; output power: 1.3 W/cm^2; Spot diameter≈10 mm). During the treatment, continuous anesthesia with isoflurane was administered, and the temperature changes at the tumor site were monitored using a thermal imaging device. Photos were taken to document the temperature changes; 4) ^{131}I-WPMNs group: dilute ^{131}I-WPMNs (11.1 MBq, 200 μL) with 0.01M PBS and administer them to the mice through the tail vein. No additional treatment should be given afterwards; 5) ^{131}I-WPMNs +Laser group: ^{131}I-WPMNs were diluted with 0.01M PBS (^{131}I: 11.1 MBq, 200 μL) and injected into the tumor-bearing mouse through the tail vein. After 24 h of injection, the tumor site was treated with an infrared laser for 20 min. Each group of mice was treated according to the requirements and placed under the same feeding conditions, providing them with the necessary water and food as mandated by animal ethics.

Statistical Analysis

The data and results were expressed with the mean or mean ± SD, and the GraphPad Prism 9.0 was used for statistical analysis. There is a significant difference when the P-value less than 0.05.

Results and Discussion
Characterization of MNPs and Mn-WPMNs

Melanin nanoparticles, as natural organic Materials, display a plethora of functional groups on their surface and possess metal chelating capabilities. In this study, we developed a multimodal probe targeting PD-L1 using established

methodologies and evaluated its utility in human lung cancer mice model characterized by elevated PD-L1 expression. We functionalized melanin nanoparticles with polyethylene glycol (PEG) and the PD-L1-targeting ligand WL12, followed by radiolabeling with the isotopes ^{89}Zr or ^{131}I. The incorporation of manganese ions (Mn^{2+}) transformed these into a multifunctional theranostic agent, designated as (^{131}I/^{89}Zr, Mn)-WPMNs. This agent leverages PD-L1 overexpression on malignant tumor cells to enable PET/MRI dual-modality imaging and combines radionuclide and photothermal therapies for a synergistic therapeutic effect.

Firstly, we successful obtain WL12-SH by chemical synthesis, the mass spectrometry and HPLC verified the molecular weight of WL12-SH was 1984.37 and purity as highly as 95% (Figure S1). Then, we conjugated WL12-SH and PEG-MNPs, which named WPMNs and the chemical structure was shown in Figure S2. The nanoparticles modified with Mn^{2+} were dispersed in solution in a spherical and monodisperse shape with uniform morphology. The dynamic light scattering (DLS), transmission electron (TEM) and near infrared spectroscopy (FT-IR) were used to character the morphology of MNPs, WPMNs and Mn-WPMNs. As shown in Figure 1A, WMNPs were spherical with particle size approximately 10 nm by conversion from the scale, and no polymerization phenomenon was observed. In the infrared spectrum, the characteristic absorption peaks at 2871 cm^{-1} and 1104 cm^{-1} in the infrared spectrum of WPMNs were due to the stretching of alkyl C-H and C-O-C of PEG molecules, while the weak peak of C-S bond at 529 cm^{-1} may be the characteristic peak of WL12-SH (Figure 1B). The hydration particle size of MNPs was 5.3±1.0 nm, the size increased to 8.5±1.3 nm after modified with WL12-SH. And the particle size of Mn-WPMNs was 13.8 ± 2.2 nm, which was larger than that of MNPs but still within the normal range (Figure 1C). The surface potentials of Mn-WPMNs were −5.1±3.3 (Figure 1D) and the stability test of Mn-WPMNs in a 0.01 M PBS and 5% HSA solution showed only approximately 10% of Mn^{2+} was released from Mn-WPMNs in both solutions after 96 hours (Figure 1F), indicating an increase binding affinity with cell membrane and great stability with biological applications. There were approximately 21 WL12-SH groups and hundreds Mn^{2+} attached to the surface of each nanoparticle. We employed X-ray photoelectron spectroscopy (XPS) to analyze the elemental composition of Mn-WPMNs. The results indicated that, beyond the elements present in WMNPs, the nanoprobes were enriched with a significant quantity of Mn^{2+} ions (Figure 1E).

Synthesis and Characterization of (^{89}Zr, Mn)-WPMNs

The high-purity solid target nuclide ^{89}Zr used for PET imaging was obtained through ^{89}Y (p, n) ^{89}Zr reaction from HM-20 medical cyclotron by the Nuclear Medicine Cyclotron Team of Peking University Cancer Hospital. Melanin nanoparticles can directly label ^{89}Zr without any chelating agents because of the numerous active conjugated groups on the surface of melanin nanoparticles with stable chemical structure (Figure S3), which eliminates the potential decrease in affinity caused by over-modification. We detected the labeling efficiency of (^{89}Zr, Mn)-WPMNs by radio-TLC with over 87% labeling rate, and the radiochemical purity increased to 95% (Figure S4 and 2A). The stability of (^{89}Zr, Mn)-WPMNs were detected by dispersing in 0.01 M PBS and 5% HSA. The radiochemical purity of ^{89}Zr-WPMNs were high than 69% and 91.44% respectively at 96 h (Figure 2B). It showed better stability in plasma than saline solution.

The pharmacokinetic test of (^{89}Zr, Mn)-WPMNs was used to investigate their affinity for circulation. As shown in Figure 2C, the data were analyzed by GraphPad Prism 9.0, and the metabolic half-life and distribution half-life were successfully calculated as 0.1234 h and 1.554 h, respectively. Then, we studied the distribution of (^{89}Zr, Mn)-WPMNs in healthy KM mice major organs. The biological distribution showed that the radioactive signals primarily accumulated in the liver (39.43±10.03%ID/g) and spleen (25.19±0.43%ID/g) after injecting (^{89}Zr, Mn)-WPMNs 24 h (Figure 2D). The results aligned with the main metabolic pathways of nanoparticles. It was worth noting that the much lower uptake of (^{89}Zr, Mn)-WPMNs in other organs (heart, lung, kidney, stomach, intestine, muscle, bone, brain), which may indicate higher security. Then, the T1WI MRI enhancement imaging and relaxation efficiency of Gd-DTPA and Mn-WPMNs at various concentrations was tested in vitro (Figure 2E). The statistical data showed that the R1 value of Mn-WPMNs was 6.74 mM^{-1} s^{-1}, which was approximately three times stronger than that of Gd-DTPA (2.33 mM^{-1} s^{-1}). (Figure 2F) These data corroborated that the (^{89}Zr, Mn)-WPMNs exhibited a high degree of labeling efficiency and robust stability, qualifying it for utilization in the multimodal imaging realms of PET and MRI.
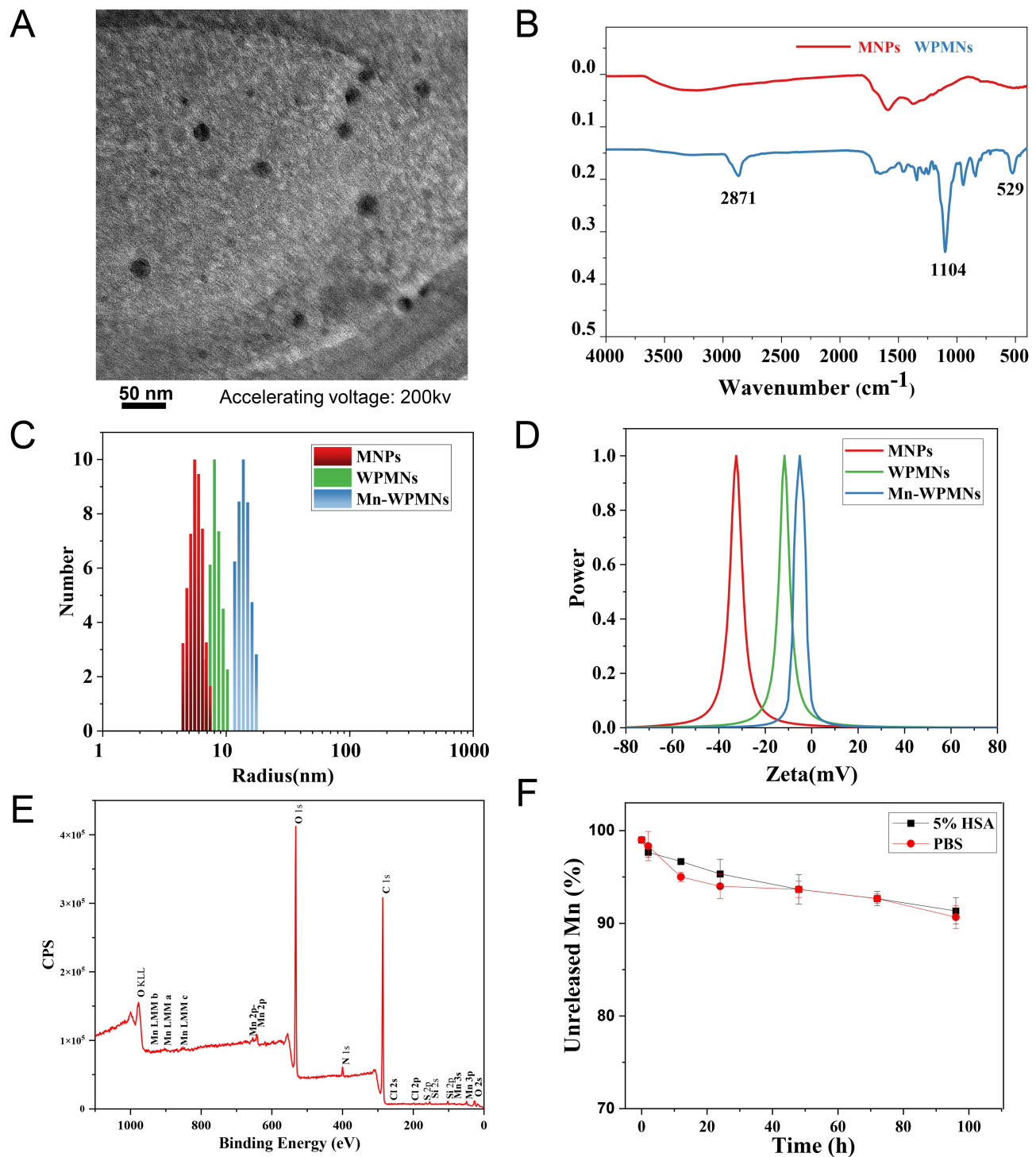
Figure 1 Characterization of the nanoparticles, all of these results are expressed as the mean ± SD. (**A**) TEM of Mn-WPMNs (scale bar = 50 nm). (**B**) FTIR spectra the MNPs (red line) and WPMNs (blue line). (**C**) Hydrodynamic particle size of MNPs (red line), WPMNs (green line), and Mn-WPMNs (blue line). (**D**) Zeta potential of MNPs (red line), WPMNs (green line), and Mn-WPMNs (blue line). (**E**) XPS detection of Mn-WPMNs. (**F**) The stability of Mn-WPMNs dispersed in 0.01 M PBS and 5% in vitro.

Cell Uptake and Micro-PET/CT Imaging in vivo

To verify the nanoprobe's PD-L1 specificity, we conducted cellular uptake assays using PD-L1-transfected A549 human lung cancer cells, performing both uptake and competitive inhibition studies. As show in Figure 3A, the uptake values of (^{89}Zr, Mn)-WPMNs in A549^{PD-L1} cells were gradually increased from 10 min to 120 min, and the highest ratio reached
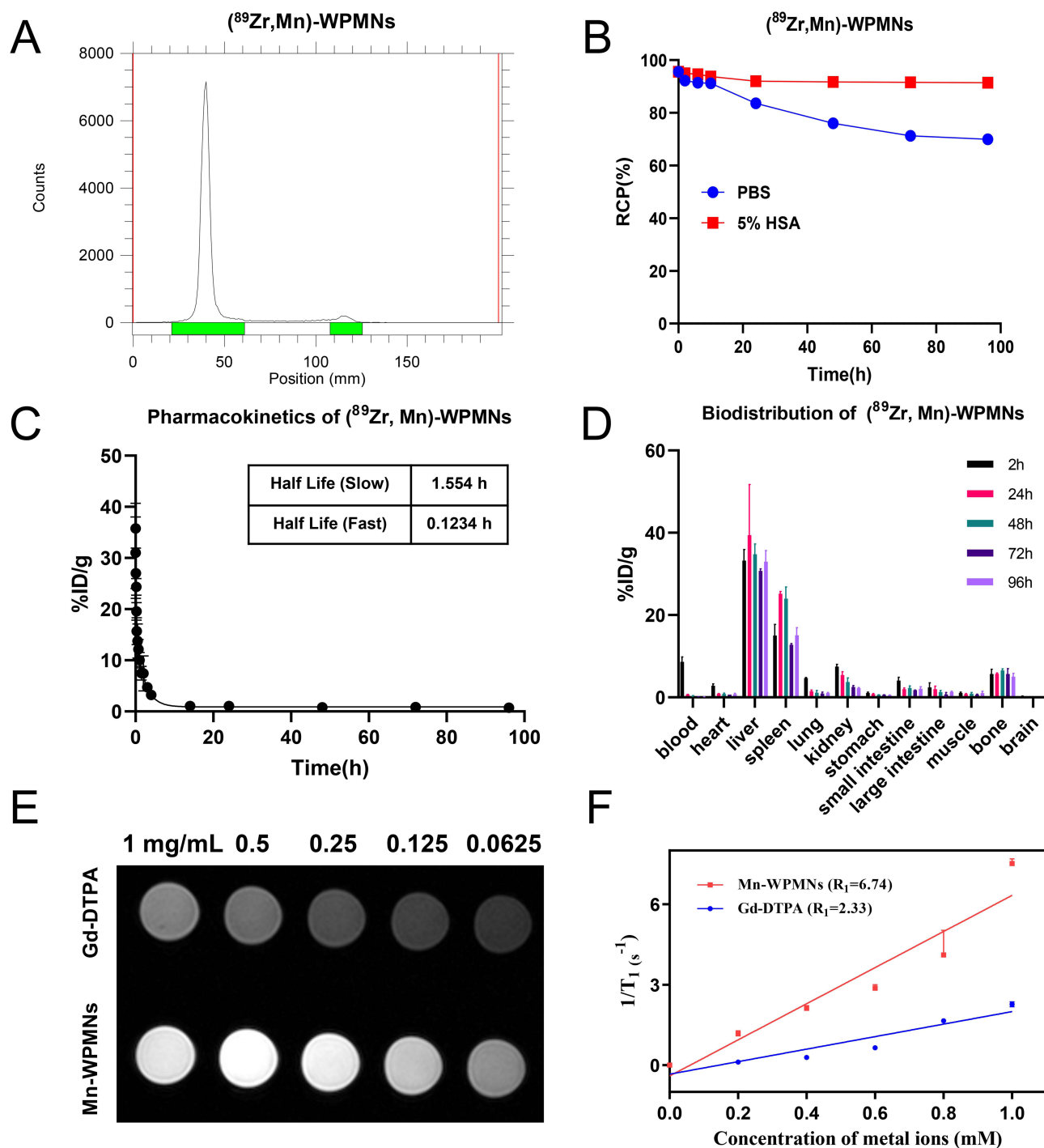
Figure 2 (**A**) Radio-TLC chromatogram of (^{89}Zr, Mn)-WPMNs after purifying. (**B**) In vitro stability of (^{89}Zr, Mn)-WPMNs in 0.01 M PBS and 5% HSA, expressed as the mean ± SD. Pharmacokinetics (**C**) and Biodistribution (**D**) of (^{89}Zr, Mn)-WPMNs, expressed as the mean ± SD. (**E**) In vitro T1-weighted MRI image with different concentrations (0.0625, 0.125, 0.25, 0.5, 1 mg/mL) of Gd-DTPA (upper levels) and Mn-WPMNs (bottom levels) (1.5 T, TR: 531 ms, TE: 9.1 ms). (**F**) The linear relationship of T1 relaxation rates (1/T_1, s^{-1}) of Mn-WPMNs (red line) and Gd-DTPA (blue line) measured in vitro, expressed as the mean ± SD.

to 1.04±0.09%IA at 2 h. The uptake ratios of (^{89}Zr, Mn)-WPMNs in A549^{PD-L1} cells with or without WPMNs blocking had significant statistical differences (1 h: 0.99±0.07%IA vs 0.48±0.01%IA, $P < 0.0001$; 2 h: 1.04±0.09%IA vs 0.56 ±0.02%IA, $P = 0.0002$). In this study, we successfully demonstrated the cellular internalization function of melanin nanoparticles for the first time, paving the way for their potential use in therapeutic applications. The results (Figure 3B) showed that the internalization rate of (^{89}Zr, Mn)-WPMNs in A549^{PD-L1} cells was descending at 4°C (from 43.32 ±
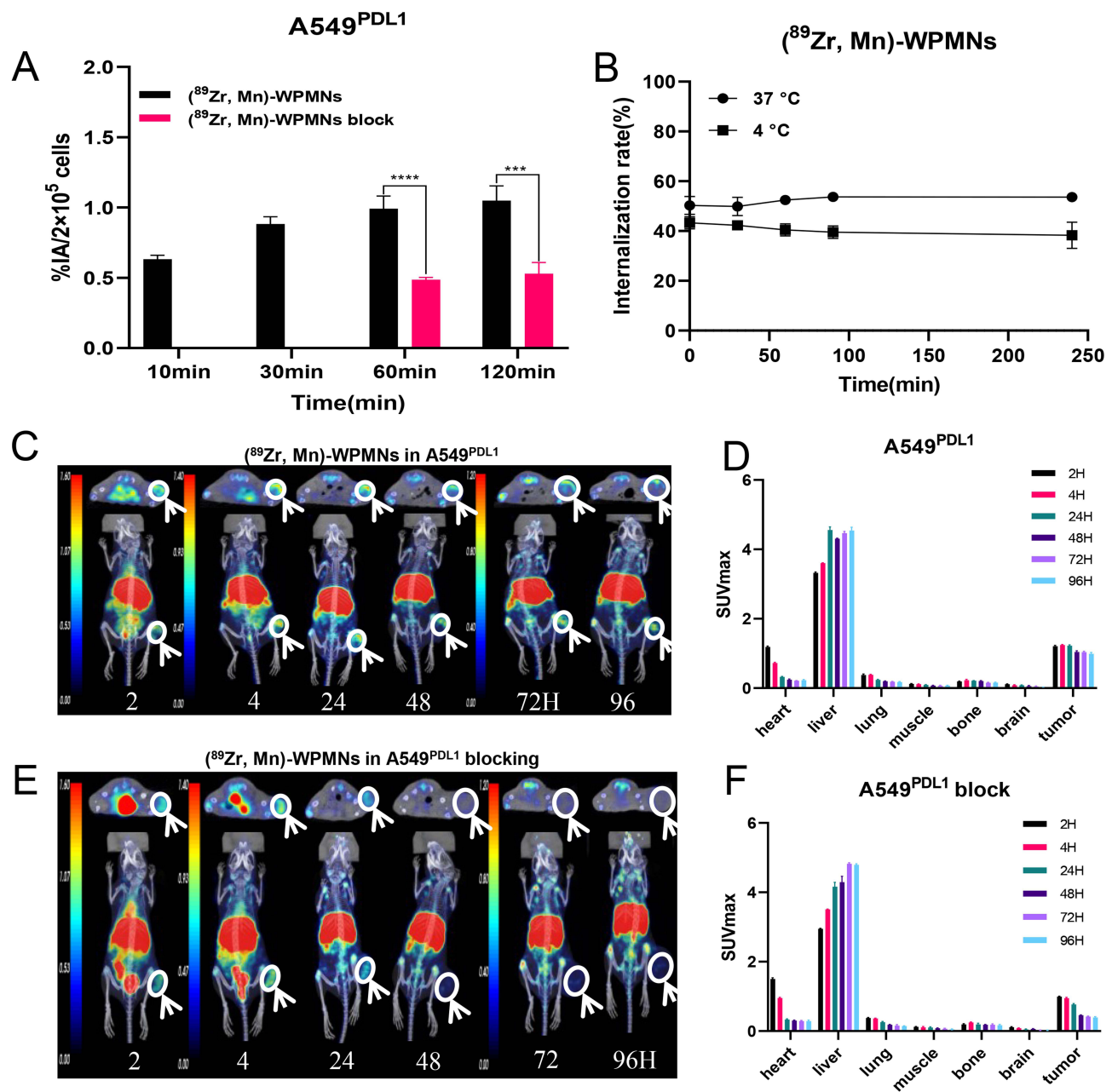
Figure 3 All of these results are expressed as the mean ± SD. Asterisk indicates ***p-value < 0.001 and ****p-value < 0.0001. (**A**) The cell uptake of (^{89}Zr, Mn)-WPMNs in A549^{PDL1} cells. (**B**) Internalization of (^{89}Zr, Mn)-WPMNs in A549^{PDL1} cells at 4°C and 37°C, respectively. (**C**) Micro-PET/CT images of A549^{PDL1} xenograft mouse after injection with (^{89}Zr, Mn)-WPMNs and (**D**) The SUVmax of the organs in the A549^{PDL1} xenograft mouse based on semi quantification of ROIs. (**E**) Micro-PET/CT images of A549^{PDL1} xenograft mouse after injection with (^{89}Zr, Mn)-WPMNs and blocking by 2.5mg/kg per mouse of Mn-WPMNs. (**F**) The SUVmax of the organs in the A549^{PDL1} mouse of blocking group based on semi quantification of ROI.

2.10% in 0 min to 38.29 ± 4.26% in 240 min) and increasing at 37°C (from 50.28 ± 3.10% to 52.46 ± 1.16%), which proved that (^{89}Zr, Mn)-WPMNs remained in cells for a long time after binding with PD-L1 and performed better at human body temperatures.

Micro-PET/CT in A549^{PD-L1} Xenograft Mice

Nuclear medicine possesses the potential to significantly enhance clinical decision-making by precisely mapping the distribution of systemic lesions. This capability is especially critical in elevating the survival rates of patients poised to receive immunotherapy. The biodistribution of (^{89}Zr, Mn)-WPMNs and their affinity for PD-L1 were investigated via

micro-PET/CT imaging following the intravenous administration of the radiotracer. As depicted in Figure 3C and E, there was an accumulation of radioactive signals in the liver and bladder across both imaging cohorts at 2 hours post injection. This observation was attributed to the inherent tendencies of (^{89}Zr, Mn)-WPMNs towards hepatic and biliary pathways, which are integral to their metabolic and excretion processes.

Furthermore, a subset of these nanoparticles was expelled via the renal-urinary pathway, which characterized by their particularly diminutive dimensions. In the non-block group, neoplastic tissue absorption rates rose sharply and remained high for over 96 hours with SUVmax values of 0.99 ± 0.02, significantly outpacing the uptake in the tumor tissues of the simultaneous blockade group (0.39 ± 0.02) (Figure 3D and F). This was due to both the high expression of PD-L1 in A549^{PD-L1} tumors and the EPR effect of nanoparticles. And we also showed its ability to target PD-L1 in vivo through blocking studies. The results showed (^{89}Zr, Mn)-WPMNs proved to have a certain retention ability in tumors. To verify the difference in signal-to-noise ratio of tumor sites between the two groups, the ratio of tumor-to-muscle and tumor-to-bone in vivo between two groups was compared (Figure S5), and all these results showed the tumor signal-to-noise ratio in the non-block group was much higher than the blocking group.

PD-L1 Targeted PET/MR Multimodal Imaging

We have verified the enhance MR imaging function of Mn-WPMNs. Compared with gadopentetic acid (Gd-DTPA), it exhibits a higher relaxation rate, proving that the probe can achieve good enhancement effects with smaller doses. The (^{89}Zr, Mn)-WPMNs possess the capability for PET/MRI dual-modal imaging, which is anticipated to enhance diagnostic accuracy and specificity. We assessed the dual-modal imaging proficiency of (^{89}Zr, Mn)-WPMNs in vivo, using the A549^{PD-L1} model. PET/MRI imaging sessions were conducted at intervals of 2, 24, 72, and 96 hours following intravenous administration. As depicted in Figure 4A1–A4, in the non-blocked group, both MRI signals and PET tracer concentrations were markedly high within tumor and liver tissues, aligning with findings from micro-PET/CT imaging analyses. Conversely, in the blocked group, MRI and PET signals were predominantly observed in the liver, with significantly reduced detection at the tumor site when compared to the non-blocked group (Figure S6B1–B4). We both delineated the SUVmax of PET and signals strength of MRI at the tumor site based on the region of interest. Both the two signals rapidly increase within 24 hours and remain for more than 96 hours. In the non-block group, the highest T/NT (tumor vs muscle) values of both types of signals at the tumor site appeared at 24 hours with 16.67 ± 3.45 of PET and 6.63 ± 0.64 of MRI (Figure 4B). The ultra-high value of T/NT reflected a better signal-to-noise ratio and better reflected the dual enhanced imaging effect. Moreover, the PET/MR signals of the non-block group were significantly higher than those of the blocking group with the T/NT of 9.58 ± 0.99 of PET and 3.54 ± 0.32 of MRI, demonstrating the PD-L1 targeted dual-model imaging ability of the (^{89}Zr, Mn)-WPMNs in vivo (Figure 4B and C).

Dual Therapy of ^{131}I-WPMNs with A549^{PD-L1} Xenograft Mice

We have confirmed the ability of the nanoprobe to target PD-L1 effectively. In an effort to engineer a probe with dual therapeutic functions, we opted for the beta-emitting therapeutic radionuclide ^{131}I over ^{89}Zr to label the WPMNs, resulting in the creation of a dual-modality therapeutic probe, ^{131}I-WPMNs, which possesses capabilities for both radionuclide therapy and photothermal therapy. Before proceeding to therapeutic experiments, we preliminarily assessed the in vivo safety profile of ^{131}I-WPMNs. Given their organic nature, melanin nanoparticles are highly biocompatible. The safety of ^{131}I-WPMNs was ascertained through the administration of 1 mg of ^{131}I-labeled WPMNs (at a radioactivity level of 1 mCi) to healthy KM mice. As shown in Figure S7, there was no significant difference in weight changes between the experimental group and the control group for 20 days of weight monitoring. In addition, HE staining of important organs (heart, liver, lung, stomach, spleen, kidney, intestines and brain) showed no significant differences between two groups at 20th day (Figure S8).

In the treatment trials, 25 A549 PD-L1 xenograft mice were randomly allocated into five groups: the control group received no specific intervention; the ^{131}I group was administered a solution of ^{131}I; the laser group underwent only laser irradiation of the tumor; the ^{131}I-WPMNs group was treated with injections of ^{131}I-labeled nanoprobe for targeted radionuclide therapy; and the ^{131}I-WPMNs+laser group received concurrent PD-L1-targeted radionuclide therapy and photothermal therapy. We initially evaluated the photothermal therapy's effectiveness by monitoring temperature increases at the tumor sites with an infrared thermometer after 808 nm laser exposure in both the Laser and ^{131}I-WPMNs+laser groups (Figure S9).
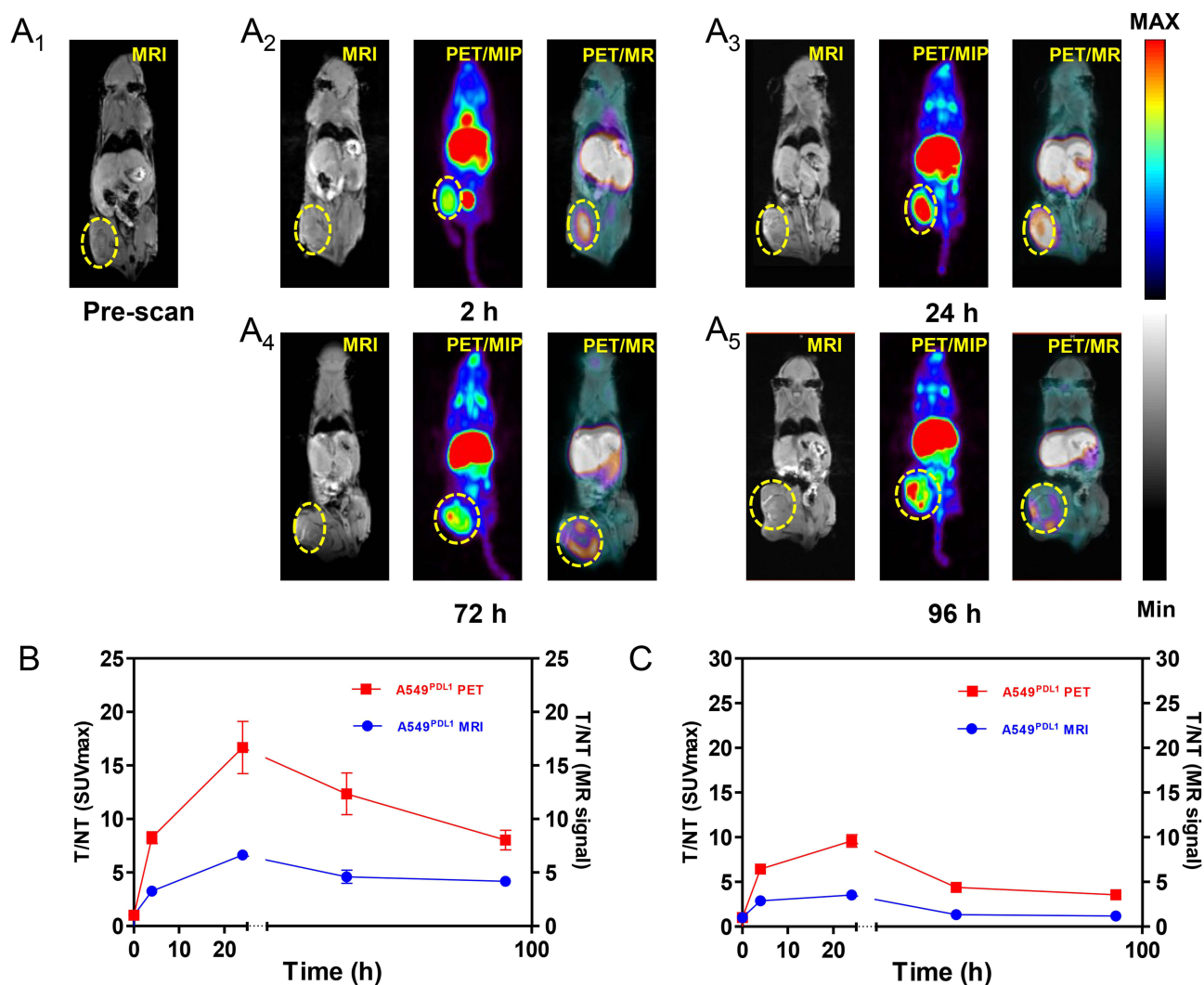
Figure 4 (**A₁–A₅**) T1-weighted MR axial images and PET/MR imaging of A549^PDL1 model before and after injection of (^89Zr, Mn)-WPMNs (tumor site enveloped by a yellow dotted line). (**B**) The distribution of PET/MRI assessed by the tumor vs muscle ratios of SUVmax and MR signal changed at non-block group as determined using the ROI, expressed as the mean ± SD. (**C**) The distribution of PET/MRI assessed by the tumor vs muscle ratios of SUVmax and MR signal changed at blocking group as determined using the ROI, expressed as the mean ± SD.

Temperatures at the tumor sites increased rapidly, with the Laser group reaching a maximum of 37.1°C, while the ^131I-WPMNs+laser group's temperature swiftly rose to 44.3°C and remained high for more than 10 minutes, suggesting a superior therapeutic effect (Figure 5A and B). In this study, we observed rapid tumor growth in A549 model tumors. The trial's duration was limited to within one week, in strict compliance with ethical guidelines. We continuously monitored the weight changes in five groups of mice and noted no significant variance in the weight change patterns (Figure 5F). Regarding therapeutic efficacy, the tumor volumes in the dual therapy group increased at a markedly slower pace than those in the control group and the other three independent treatment groups (Figure 5D). By the end of the study, the tumor weights in the dual therapy group were significantly lower than those in the other groups, presenting a statistically significant difference (Figure 5C and E). Despite the treatment duration constraints, the aggregated statistical evidence supports the conclusion that the dual-functional therapeutic regimen effectively inhibited tumor proliferation. Notably, the group treated with ^131I-WPMNs for targeted radionuclide therapy exhibited a superior treatment outcome compared to the group receiving non-targeted ^131I therapy. This outcome aligns with the study's initial expectations. The findings established a solid groundwork for the future development of an integrated diagnostic and treatment platform.
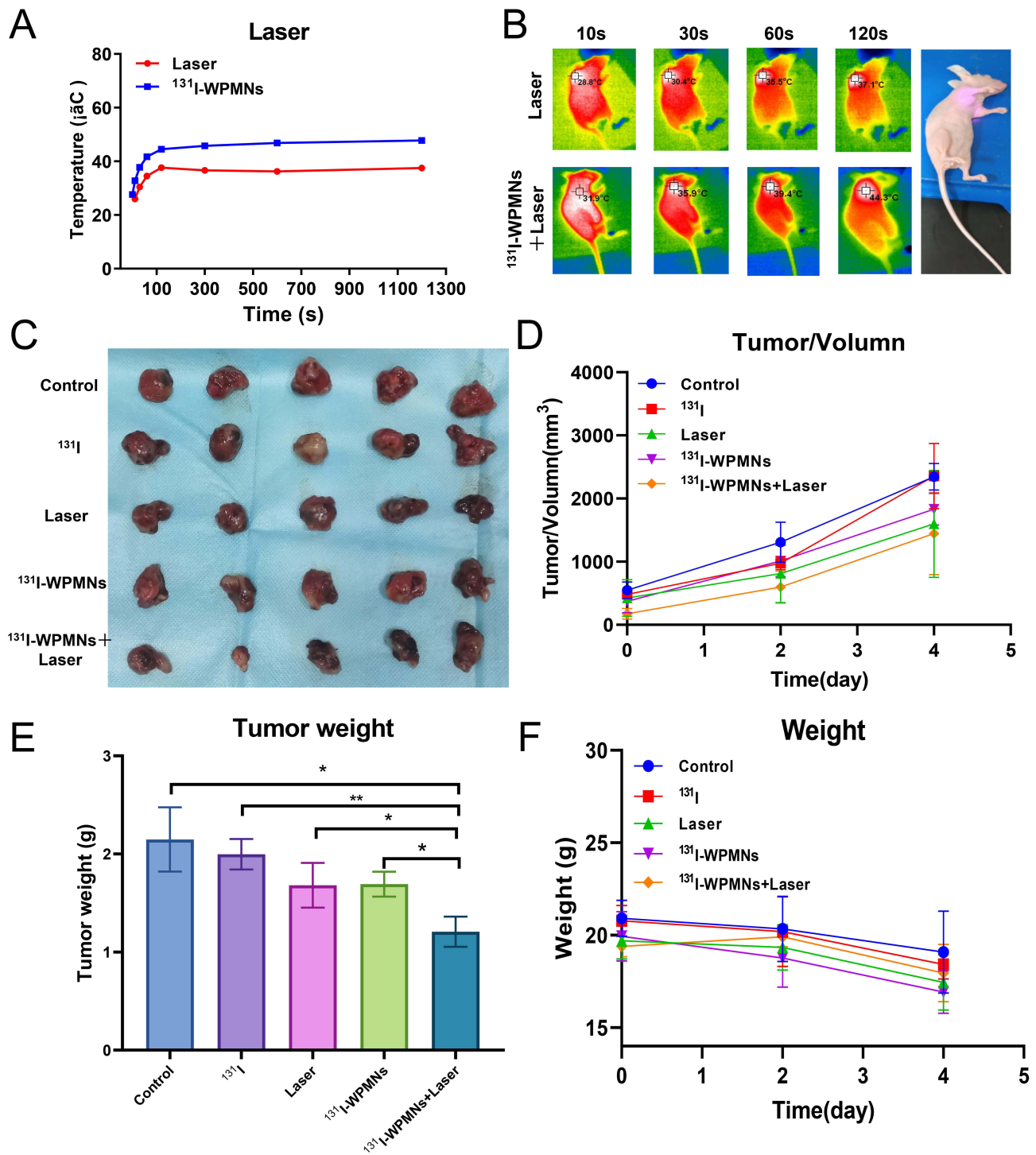
Figure 5 All of these results are expressed as the mean ± SD. Asterisk indicates *p-value < 0.05 and **p-value < 0.01. (**A**) Changes in tumor temperature in two groups treated with photothermal therapy upon exposure to the NIR (Near-Infrared) laser. (**B**) Infrared thermal images depicting the temperature evolution of mice in two photothermal therapy groups over 120 seconds, highlighting the tumor-bearing areas. (**C**) Photographic documentation of tumors from each experimental group on the final day of treatment, n=5. (**D**) Temporal progression curves illustrating changes in tumor volume across the five experimental groups, n=5. (**E**) Comparative statistics of tumor weights from each group measured on the last day of treatment, n=5. (**F**) Temporal progression curves depicting variations in body weight for each mouse group throughout the treatment period, n=5.

Conclusion

Overall, we have developed a theranostic nanoprobe with high specificity for targeting PD-L1, which was conducive to enhanced dual-modality imaging via PET/MRI and was apt for precision tumor-targeted radionuclide and photothermal therapies. The nanoprobe demonstrates superior stability both in vitro and in vivo, with commendable biocompatibility and safety profiles. The cellular and animal studies have confirmed the probe's targeted tumor specificity and its exceptional imaging capabilities. The efficaciousness of the (^{89}Zr, Mn)-WPMNs was underscored by Micro-PET/CT and PET/MRI imaging data, evidencing excellent imaging quality and a notable tumor-to-background signal ratio. The therapeutic potential of ^{131}I-WPMNs had been validated through treatment trials, where significantly impeded tumor growth promptly through synergistic radionuclide and photothermal therapeutic actions. The construct of this theranostic nanoprobe could address prevalent clinical hurdles like drug resistance and difficulties in treatment monitoring inherent in PD-L1-targeted therapies. It offers a promising new avenue for the diagnosis and treatment of patients with resistance to immunotherapy. Going forward, our research will delve into the potential of this platform to enhance the adjunctive treatment with PD-1/PD-L1 inhibitors and to facilitate the real-time visualization of therapeutic responses.

Disclosure

The authors report no conflicts of interest in this work.

References

1. Ribas A, Hamid O, Daud A, et al. Association of pembrolizumab with tumor response and survival among patients with advanced melanoma. *JAMA*. 2016;315(15):1600–1609. doi:10.1001/jama.2016.4059
2. Reck M, Rodríguez-Abreu D, Robinson AG, et al. Pembrolizumab versus chemotherapy for PD-L1–positive non–small-cell lung cancer. *N Engl J Med*. 2016;375(19):1823–1833. doi:10.1056/NEJMoa1606774
3. Motzer RJ, Escudier B, McDermott DF, et al. Nivolumab versus everolimus in advanced renal-cell carcinoma. *N Engl J Med*. 2015;373 (19):1803–1813. doi:10.1056/NEJMoa1510665
4. Ratajczak K, Grel H, Olejnik P, Jakiela S, Stobiecka MJB. Bioelectronics Current progress, strategy, and prospects of PD-1/PDL-1 immune checkpoint biosensing platforms for cancer diagnostics, therapy monitoring, and drug screening. *Biosensors & Bioelectronics*. 2023;240:115644. doi:10.1016/j.bios.2023.115644
5. Chen S, Crabill GA, Pritchard TS, et al. Mechanisms regulating PD-L1 expression on tumor and immune cells. *J Immunother Cancer*. 2019;7:1–12.
6. Herbst RS, Soria J-C, Kowanetz M, et al. Predictive correlates of response to the anti-PD-L1 antibody MPDL3280A in cancer patients. *Nature*. 2014;515(7528):563–567. doi:10.1038/nature14011
7. Hirsch FR, McElhinny A, Stanforth D, et al. PD-L1 immunohistochemistry assays for lung cancer: results from Phase 1 of the blueprint PD-L1 IHC assay comparison project. *Journal of Thoracic Oncology: Official Publication of the International Association for the Study of Lung Cancer*. 2017;12(2):208–222. doi:10.1016/j.jtho.2016.11.2228
8. Restifo NP, Smyth MJ, Snyder A. Acquired resistance to immunotherapy and future challenges. *Nat Rev Cancer*. 2016;16(2):121–126. doi:10.1038/ nrc.2016.2
9. Arasanz H, Bocanegra AI, Morilla I, et al. Circulating low density neutrophils are associated with resistance to first line anti-Pd1/Pdl1 immunotherapy in non-small cell lung cancer. *Cancers*. 2022;14(16):3846. doi:10.3390/cancers14163846
10. Lei Q, Wang D, Sun K, Wang L, Zhang Y. Resistance mechanisms of anti-PD1/PDL1 therapy in solid tumors. *Front Cell Develop Biol*. 2020;8:672. doi:10.3389/fcell.2020.00672
11. Zaretsky JM, Garcia-Diaz A, Shin DS, et al. Mutations associated with acquired resistance to PD-1 blockade in melanoma. *N Engl J Med*. 2016;375 (9):819–829. doi:10.1056/NEJMoa1604958
12. Tumeh PC, Harview CL, Yearley JH, et al. PD-1 blockade induces responses by inhibiting adaptive immune resistance. *Nature*. 2014;515 (7528):568–571. doi:10.1038/nature13954
13. Topalian SL, Taube JM, Anders RA, Pardoll DM. Mechanism-driven biomarkers to guide immune checkpoint blockade in cancer therapy. *Nat Rev Cancer*. 2016;16(5):275–287. doi:10.1038/nrc.2016.36
14. Le DT, Durham JN, Smith KN, et al. Mismatch repair deficiency predicts response of solid tumors to PD-1 blockade. *Science*. 2017;357 (6349):409–413. doi:10.1126/science.aan6733

15. Patel SJ, Sanjana NE, Kishton RJ, et al. Identification of essential genes for cancer immunotherapy. *Nature*. 2017;548(7669):537–542. doi:10.1038/nature23477

16. Larkin J, Chiarion-Sileni V, Gonzalez R, et al. Five-year survival with combined nivolumab and ipilimumab in advanced melanoma. *N Engl J Med*. 2019;381(16):1535–1546. doi:10.1056/NEJMoa1910836

17. Postow MA, Sidlow R, Hellmann MD. Immune-related adverse events associated with immune checkpoint blockade. *N Engl J Med*. 2018;378(2):158–168. doi:10.1056/NEJMra1703481

18. Cunningham D, Allum WH, Stenning SP, et al. Perioperative chemotherapy versus surgery alone for resectable gastroesophageal cancer. *N Engl J Med*. 2006;355(1):11–20. doi:10.1056/NEJMoa055531

19. Chargari C, Levy A, Paoletti X, et al. Methodological development of combination drug and radiotherapy in basic and clinical research. *Clin Cancer Res*. 2020;26(18):4723–4736. doi:10.1158/1078-0432.CCR-19-4155

20. Al-Lazikani B, Banerji U, Workman P. Combinatorial drug therapy for cancer in the post-genomic era. *Nature Biotechnol*. 2012;30(7):679–692. doi:10.1038/nbt.2284

21. Zhou X, Jiang J, Yang X, et al. First-in-Humans evaluation of a PD-L1–binding peptide PET radiotracer in non–small cell lung cancer patients. *J Nucl Med*. 2022;63(4):536–542. doi:10.2967/jnumed.121.262045

22. Xia L, He C, Guo Y, et al. Preparation and Application of a Bioorganic Nanoparticle-Enhanced PDL1-Targeted Small-Molecule Probe. *ACS Appl Mater Interfaces*. 2023;15(25):30619–30629.

23. Kastelik-Hryniewiecka A, Jewula P, Bakalorz K, Kramer-Marek G, Kuźnik N. Targeted PET/MRI imaging super probes: a critical review of opportunities and challenges. *Int j Nanomed*. 2022;Volume 16:8465–8483. doi:10.2147/IJN.S336299

24. Smeraldo A, Ponsiglione AM, Soricelli A, Netti PA, Torino E. Update on the Use of PET/MRI Contrast Agents and Tracers in Brain Oncology: a Systematic Review. *Int j Nanomed*. 2022;17:3343. doi:10.2147/IJN.S362192

25. Harat M, Rakowska J, Harat M, et al. Combining amino acid PET and MRI imaging increases accuracy to define malignant areas in adult glioma. *Nat Commun*. 2023;14(1):4572. doi:10.1038/s41467-023-39731-8

26. Xia L, Meng X, Wen L, et al. A highly specific multiple enhancement theranostic nanoprobe for PET/MRI/PAI image-guided radioisotope combined photothermal therapy in prostate cancer. *Small*. 2021;17(21):2100378. doi:10.1002/smll.202100378

27. Tu Y, Ma X, Chen H, et al. Molecular imaging of matrix metalloproteinase-2 in atherosclerosis using a smart multifunctional PET/MRI nanoparticle. *Int j Nanomed*. 2022;17:6773. doi:10.2147/IJN.S385679

28. Xia L, Wen L, Meng X, et al. Application analysis of 124I-PPMN for enhanced retention in tumors of prostate cancer xenograft mice. *Int j Nanomed*. 2021;Volume 16:7685–7695. doi:10.2147/IJN.S330237